

Supplementary Material

Fabrication of nanoparticle array membranes by integrating semi-crystalline polymer self-assembly with NIPS for water treatment

Yu Ma^{a, b}, Xiaoli Zhao^{c *}, Bin He^{a, b *}

^a Guangdong Key Laboratory of Integrated Agro-environmental Pollution Control and Management, Guangdong Institute of Eco-environmental Science & Technology, Guangzhou 510650, China.

^b National-Regional Joint Engineering Research Center for Soil Pollution Control and Remediation in South China, Guangzhou 510650, China.

^cState Key Laboratory of Environmental Criteria and Risk Assessment, Chinese Research Academy of Environmental Sciences, Beijing 100012, China

* Corresponding author. Email: zhaoxiaoli_zxl@126.com, bhe@soil.gd.cn

Contents

1. Fabrication procedure of the PVDF nanoparticle array (NPs-A) membrane.....	5
2. Morphologies of the membranes through the fabrication procedure.....	6
3. Mechanism of the membrane fabrication procedure	8
3.1 Explanation of the PVDF crystal structures uniformly distributed in PVDF-S membrane.....	9
4. Parameters of the NPs-A membranes.	12
5. Separation performances of the 9-NPs-A membranes.....	13
5.1 Calculation method.....	13
References.....	22

Figures

Figure S1. Tyndall effect in the PVDF NPs dispersion	5
Figure S2. Size/concentration distribution of the PVDF NPs dispersion tested by a NP tracking analyzer (The adding volume of the PVDF solution to the water are 0.5, 1, and 2 mL).....	5
Figure S3. SEM image of the surface morphology of the PVDF-C membranes.....	6
Figure S4. SEM image of the surface and cross-section morphology of the PVDF-S5 membrane.....	6
Figure S5. STEM image of the PVDF-S20 membrane.....	7
Figure S6. SEM images of PVDF-NPs10 membrane (a) and PVDF-NPs20 membrane (b)	7
Figure S7. X-ray diffraction (XRD) patterns of PVDF-C5, PVDF-C8, PVDF-C10, PVDF-C20	8
Figure S8. PVDF polymer draw and form threads in poor phase.....	8
Figure S9. Variation of DMF concentration with Arc length.	10
Figure S10. Cross-sectional images of the 30-NPs-A5 membrane.....	11
Figure S11. (a) Cross-sectional images of the 0-NPs-A5 membrane; (b) Pore-size distribution of the 0-NPs-A5 membrane; (c) Cross-sectional images of the 5-NPs-A5 membrane; (d) Pore-size distribution of the 5-NPs-A5 membrane.	12
Figure S12. Comparison of the pore size distribution in membranes fabricated through block copolymer self-assembly versus those produced by non-solvent induced phase separation (SNIPS). (a) This work; (b) Membrane formed by using micelle-forming amphiphilic block copolymer (BCP) of poly(ethylene oxide) (PEO) and poly[3-(trimethoxysilyl)propyl methacrylate] (PTMSPMA), PEO114- <i>b</i> -PTMSPMA228 ² ; (c) Membrane formed by using Polystyrene- <i>block</i> -poly (acrylic acid) (PS- <i>b</i> -PAA) diblock copolymers ³ ; (d) Membrane formed by using poly(<i>n</i> -isopropylacrylamide)- <i>b</i> -poly(vinylidene fluoride) copolymer, (PNIPAM- <i>b</i> -PVDF) ⁴ ; (e) Membrane formed by using Polystyrene- <i>block</i> -poly (acrylic acid) (PS- <i>b</i> -PAA) copolymer ⁵ ; (f) Membrane formed by using polysulfone- <i>block</i> -polyethylene glycol (PSf- <i>b</i> -PEG) block copolymer ⁶	12
Figure S13. The Zeta potential of the 9-NPs-A5 membrane (ζ^m)	16
Figure S14. The Zeta potential of the polystyrene (PS) microspheres (ζ^p).	17
Figure S15. The rejection rates of polystyrene microspheres for the 9-NPs-A membranes. The particle size is 700 nm (a) and 1000 nm (b)	20
Figure S16. (a, c) AFM images of 9-NPs-A5 membrane (a) and commercial PVDF membrane (c); (b, d) DMT modulus of the 9-NPs-A5 membrane (b) and commercial PVDF membrane (d) (PF-QNM mode, AFM).....	21
Figure S17. Standard curve of fluorescence intensity at 433 nm versus concentrations of 500 nm (a), 700 nm (b), and 1000 nm (c) polystyrene microspheres.....	22

Tables

Table S1. Parameters of the NPs-A membranes	12
Table S2. Performance comparison of current PVDF-based separation membranes with similar pore size	17

1. Fabrication procedure of the PVDF nanoparticle array (NPs-A) membrane

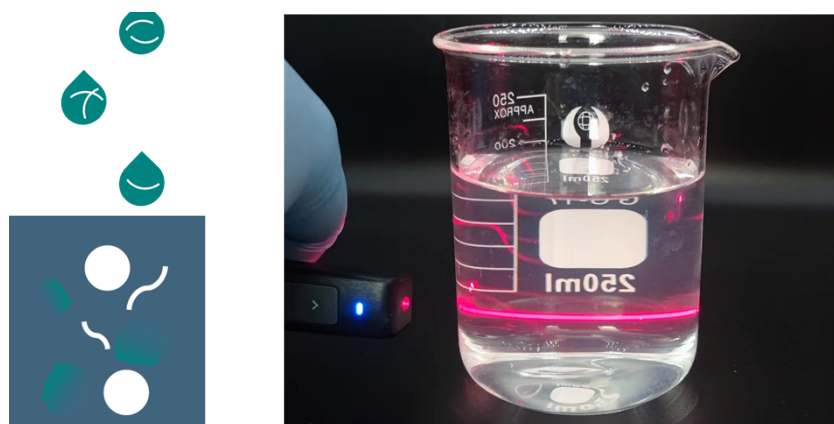


Figure S1. Tyndall effect in the PVDF NPs dispersion

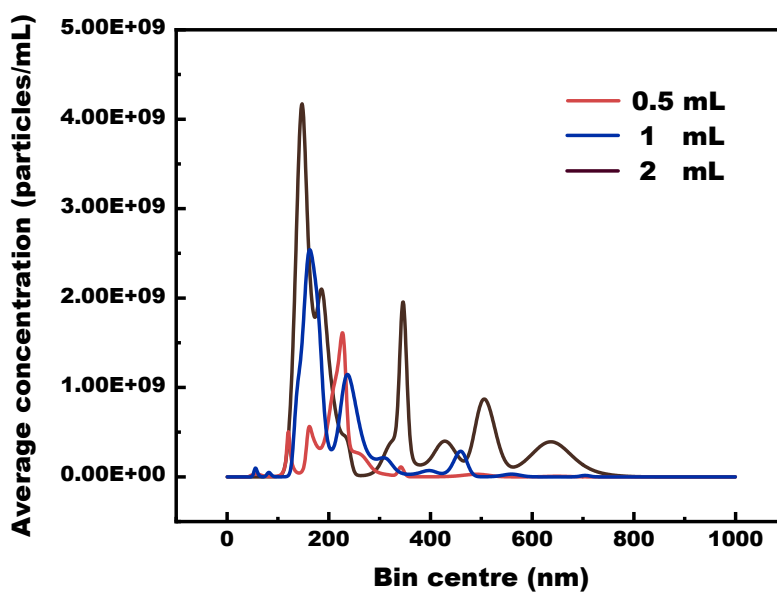


Figure S2. Size/concentration distribution of the PVDF NPs dispersion tested by a NP tracking analyzer (The adding volume of the PVDF solution to the water are 0.5, 1, and 2 mL)

2. Morphologies of the membranes through the fabrication procedure

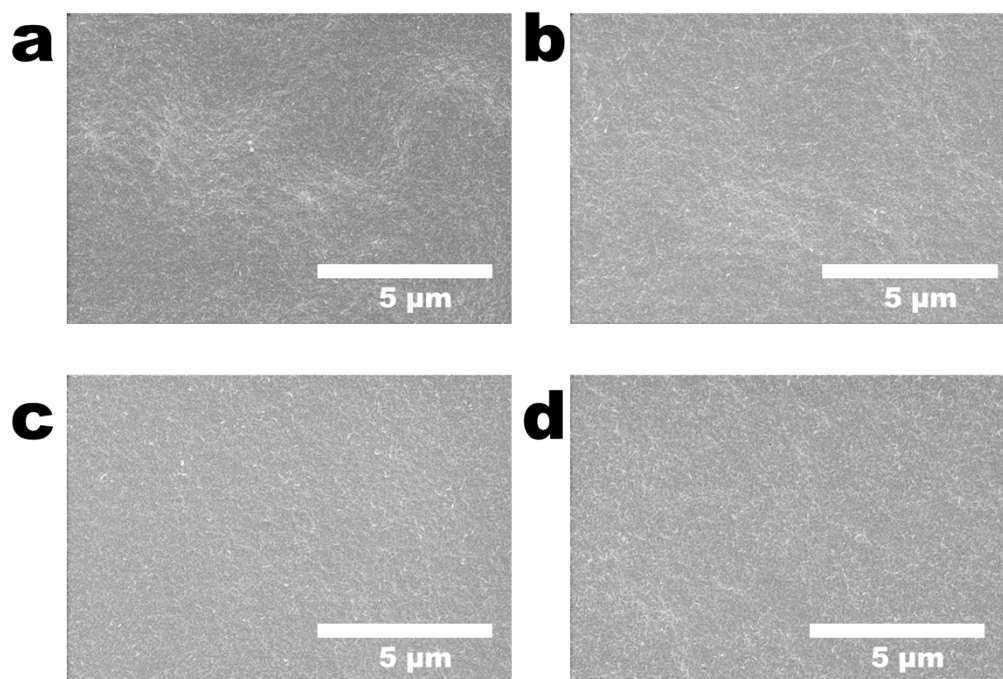


Figure S3. SEM image of the surface morphology of the PVDF-C membranes

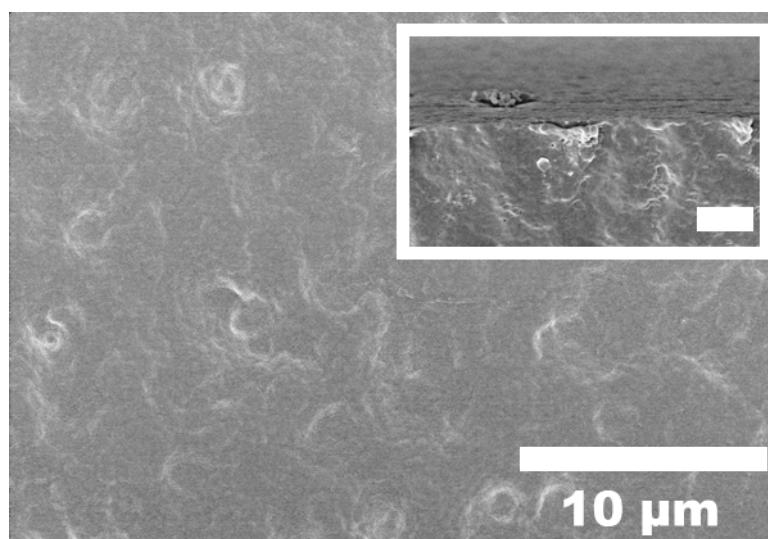


Figure S4. SEM image of the surface and cross-section morphology of the PVDF-S5 membrane

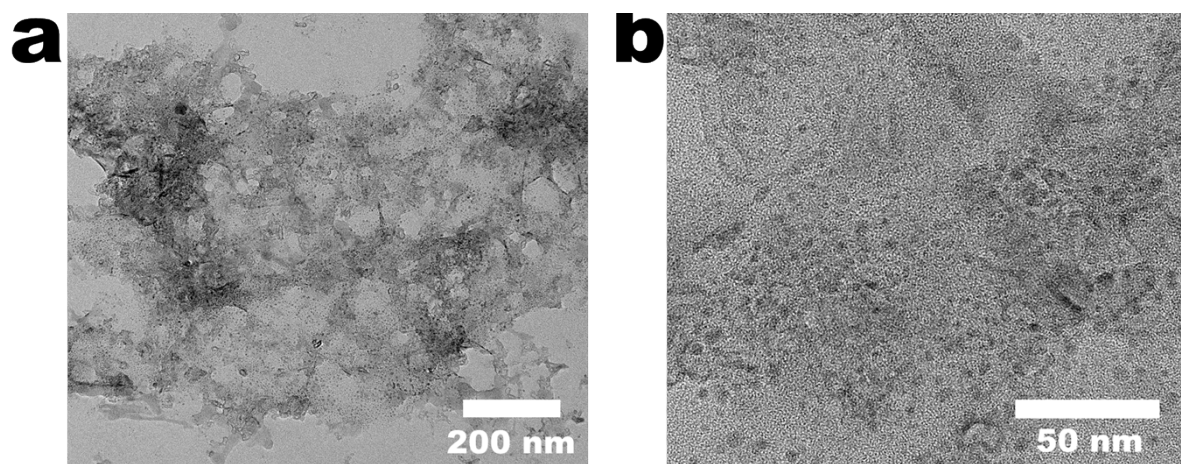


Figure S5. STEM image of the PVDF-S20 membrane

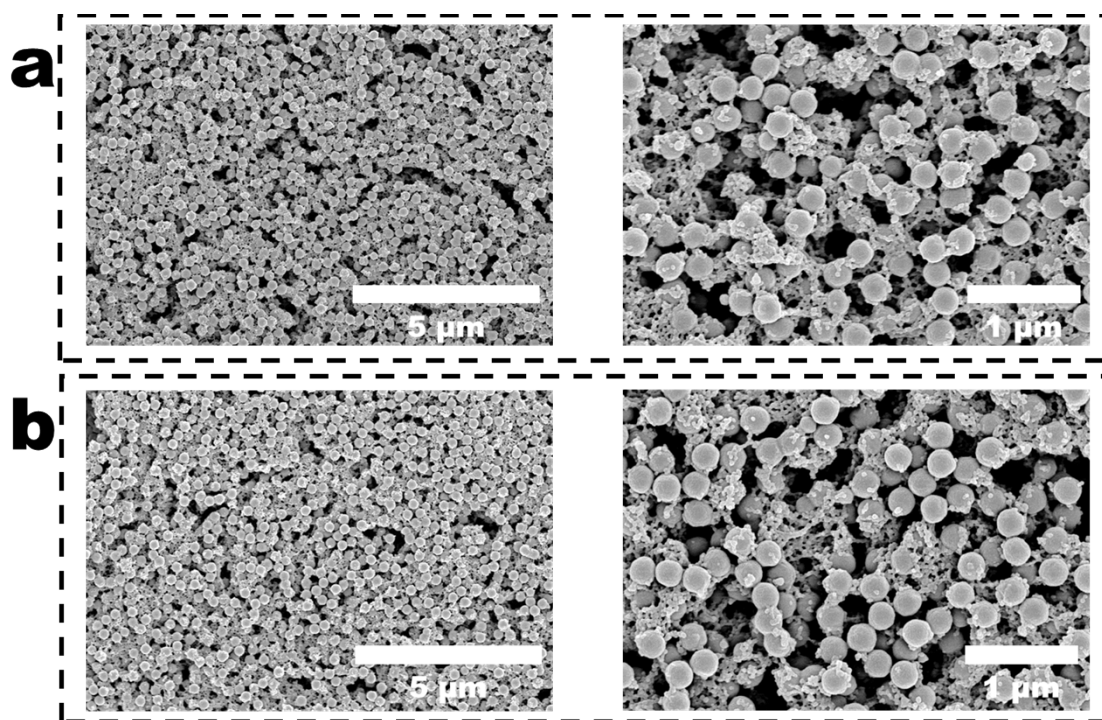


Figure S6. SEM images of PVDF-NPs10 membrane (a) and PVDF-NPs20 membrane (b)

3. Mechanism of the membrane fabrication procedure

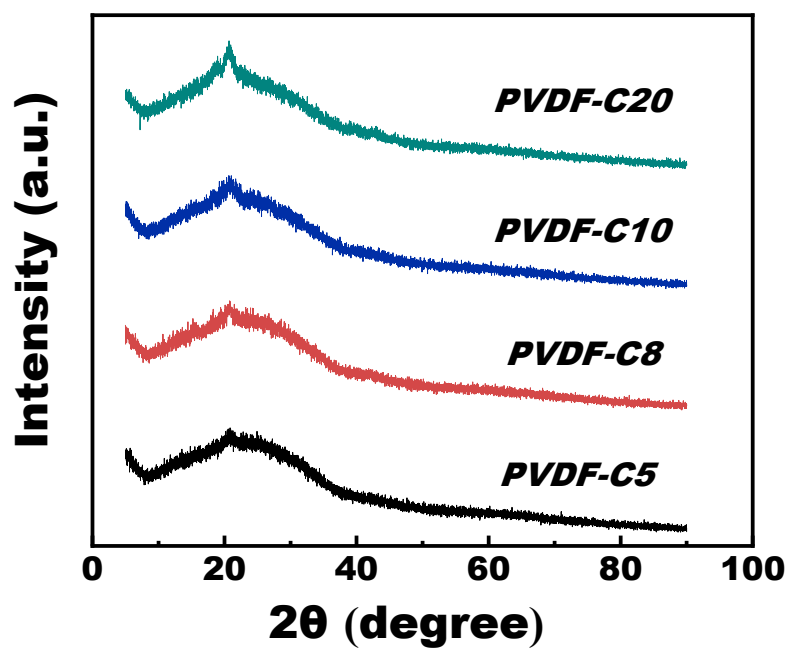


Figure S7. X-ray diffraction (XRD) patterns of PVDF-C5, PVDF-C8, PVDF-C10, PVDF-C20

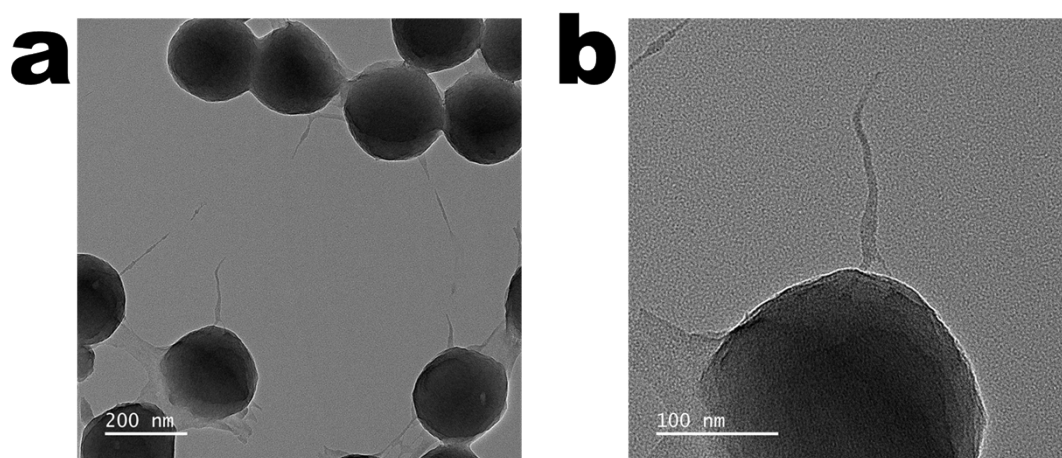


Figure S8. PVDF polymer draw and form threads in poor phase.

3.1 Explanation of the PVDF crystal structures uniformly distributed in PVDF-S membrane

Due to concentration differences, DMF undergoes diffusion during the filtration process, and the diffusion process is driven by the chemical potential gradient, which generates a driving force for DMF transfer. Therefore, the direction of the force is isotropic, allowing DMF to be transferred in all directions within the membrane with equal probability, ultimately leading to even distribution. Additionally, as the pressure was homogeneous throughout the membrane during filtration, the force that drives DMF into the membrane was homogeneous in a single direction. Due to the simultaneous occurrence of diffusion and pressure-driven mechanisms, the resulting force can be expressed as ¹ :

$$p_t = \Delta p + \Delta \pi = - \frac{RT \ln \left(1 - \frac{J \Delta x}{DKc} \right)}{V} > \Delta p \quad (\text{S1})$$

$$D = \frac{kT}{6\pi\mu r} \quad (\text{S2})$$

In the equation, p_t represents the pressure that drives the transfer of DMF, Δp represents the vacuum pressure, $\Delta \pi$ represents the osmotic pressure generated during the diffusion process, R is the ideal gas constant, T is temperature, J is the permeation flux of DMF, Δx is the membrane thickness, D is the diffusion coefficient of DMF, K is the distribution coefficient, c is the molar concentration of DMF in the membrane, k is the Boltzmann constant, μ is the viscosity of DMF, and r is the radius of DMF molecules. It can be seen that during the diffusion process of DMF, a driving force greater than the vacuum pressure (0.95 bar) can be generated in the membrane to drive DMF transfer. The transfer of DMF can also cause migration of polymer segments and crystal types inside the viscous PVDF-C membrane (with a viscosity of 874 Pa·s).

This study uses COMSOL Multiphysics to simulate the transfer path of DMF inside the membrane. Specifically, the Convection-Diffusion equation and Navier-Stokes equation were used for description:

$$\frac{\partial c}{\partial t} + \nabla(-D\nabla c + uc) = \alpha \quad (\text{S3})$$

$$\underbrace{\rho \left(\frac{\partial \mathbf{u}}{\partial t} + \mathbf{u} \cdot \nabla \mathbf{u} \right)}_1 = \underbrace{-\nabla p}_2 + \underbrace{\nabla \cdot (\mu(\nabla \mathbf{u} + (\nabla \mathbf{u})^T) - \frac{2}{3}\mu(\nabla \cdot \mathbf{u})\mathbf{I})}_3 \quad (\text{S4})$$

In the equation, $u = (u_x, u_y, u_z)$ represents the mass transfer rate of DMF in different directions, t is the time, α is called the reaction term, ρ is the density of DMF, and $\nabla p = (p_x, p_y, p_z)$ represents the pressure applied to DMF in different directions. In **Equation S4**, the different terms

correspond to inertial forces (1), pressure forces (2), and viscous forces (3). By providing the diffusion rate of DMF ($1.54E^{-9} \text{ m}^2 \cdot \text{s}^{-1}$), vacuum pressure, and the viscosity of the PVDF-S membrane, the diffusion pathway of DMF within the membrane can be simulated. As shown in **Figure 3i** and **Figure S9**, DMF diffuses uniformly in all directions within the PVDF-S membrane, leading to a uniformly distributed DMF in the membrane. As a result, the chemical-potential gradient of DMF diffusion, and pressure propels crystal structures to move, ultimately leading them to be uniformly distributed within the membrane.

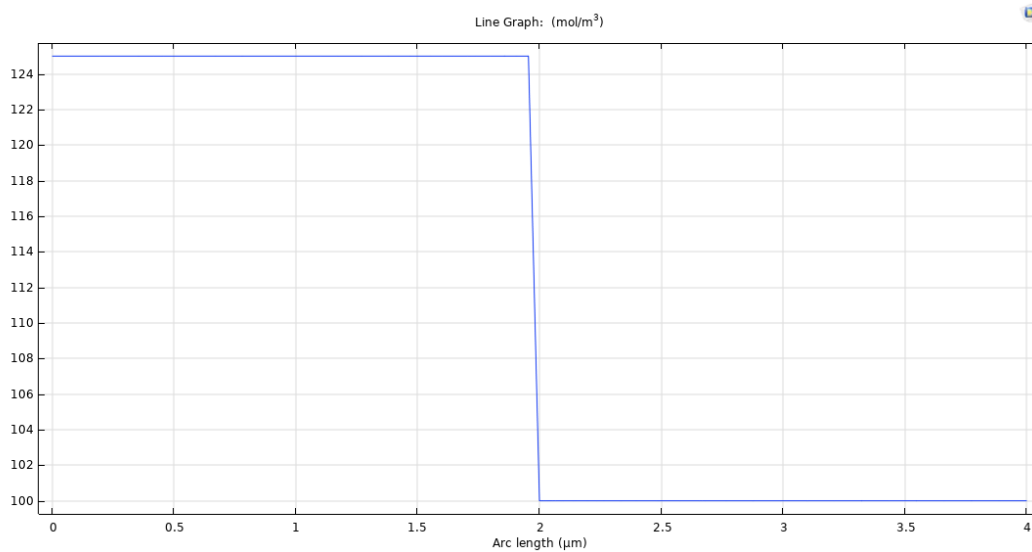


Figure S9. Variation of DMF concentration with Arc length.

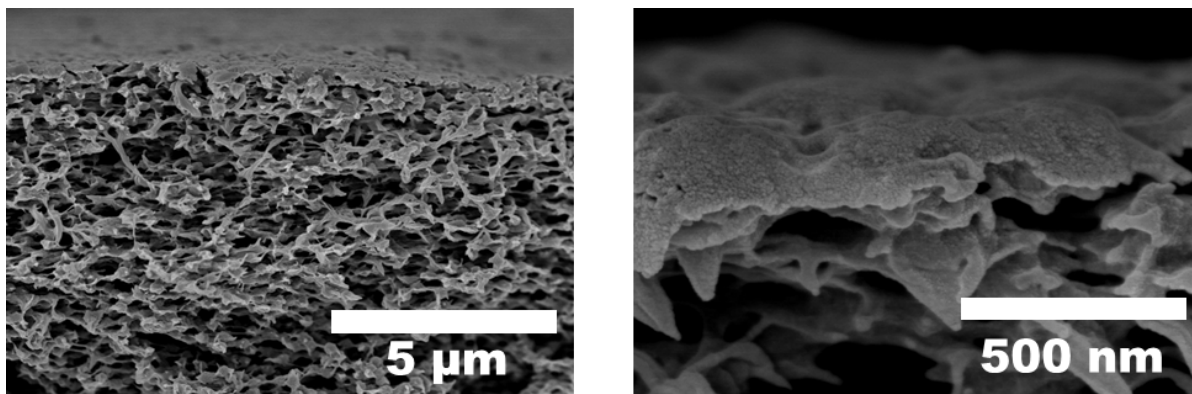


Figure S10. Cross-sectional images of the 30-NPs-A5 membrane.

4. Parameters of the NPs-A membranes.

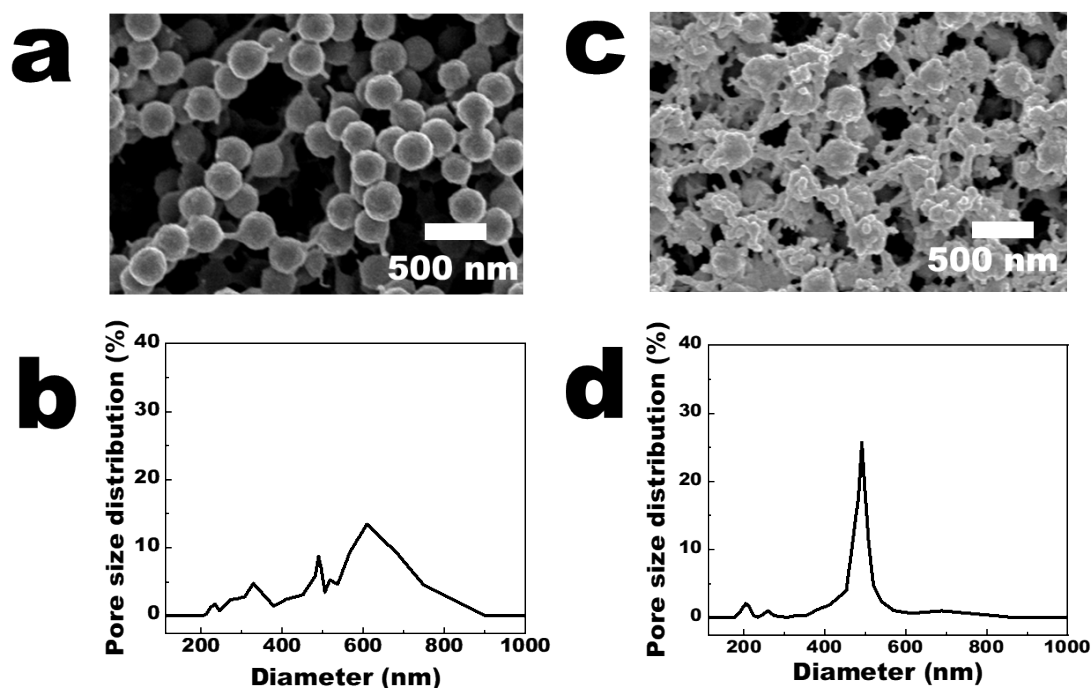


Figure S11. (a) Cross-sectional images of the 0-NPs-A5 membrane; (b) Pore-size distribution of the 0-NPs-A5 membrane; (c) Cross-sectional images of the 5-NPs-A5 membrane; (d) Pore-size distribution of the 5-NPs-A5 membrane.

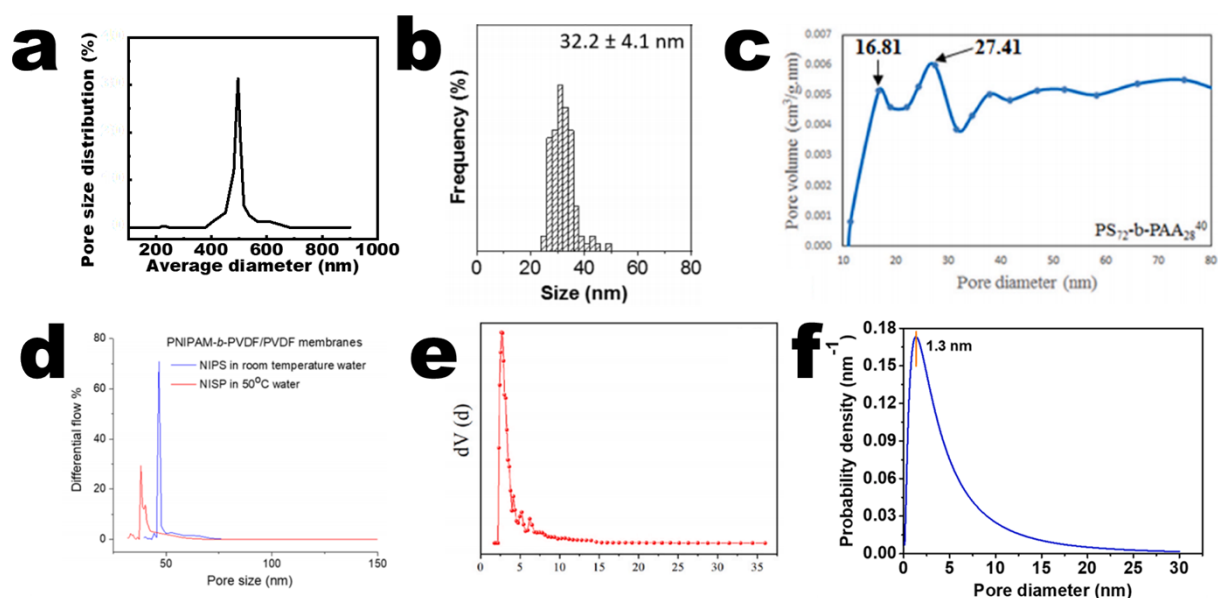


Figure S12. Comparison of the pore size distribution in membranes fabricated through block copolymer self-assembly with non-solvent induced phase inversion (SNIPS). (a) This work; (b) Membrane formed by using micelle-forming amphiphilic block copolymer (BCP) of poly(ethylene oxide) (PEO) and poly[3-(trimethoxysilyl)propyl methacrylate] (PTMSPMA), PEO114-*b*-PTMSPMA228²; (c) Membrane formed by using Polystyrene-*block*-poly (acrylic

acid) (PS-*b*-PAA) diblock copolymers³; (d) Membrane formed by using poly(*n*-isopropylacrylamide)-*b*-poly(vinylidene fluoride) copolymer, (PNIPAM-*b*-PVDF)⁴; (e) Membrane formed by using Polystyrene-*block*-poly (acrylic acid) (PS-*b*-PAA) copolymer⁵; (f) Membrane formed by using polysulfone-*block*-polyethylene glycol (PSf-*b*-PEG) block copolymer⁶.

Table S1. Parameters of the NPs-A membranes

Membrane	Average pore size (nm)	Thickness (μm)	Porosity (%)
9-NPs-A5	523	~1.94	87.06
0-NPs-A5	694	~4.11	93.55
5-NPs-A5	539	~2.83	84.37
9-NPs-A8	517	~3.75	72.38
9-NPs-A10	500	~5.41	46.08
9-NPs-A20	491	~11.33	38.42

5. Separation performances of the 9-NPs-A membranes

5.1 Calculation method

According to the Hagen-Poiseuille equation (**Equation 2**), the membrane flux J is directly related to the membrane thickness, porosity, and pore size. Since the Hagen-Poiseuille equation assumes the channels within the membrane to be vertical cylinders and neglects the resistive effects of the tortuosity of the internal channels, a tortuosity parameter η is introduced into the Hagen-Poiseuille equation. The tortuosity parameter is calculated based on the experimental flux of the 9-NPs-A5 membrane and is then used in combination with the data from **Table S1** to calculate the theoretical fluxes for other 9-NPs-A membranes. Since the tortuosity parameter of all 9-NPs-A membranes is assumed to be the same as that of the 9-NPs-A5 membrane in the calculation process, the calculated theoretical fluxes for all membranes are assumed to be the same as the tortuosity of the 9-NPs-A5 membrane. Therefore, by comparing the calculated results with the experimental flux of the membranes, the effect of the pore tortuosity on membrane flux can be intuitively reflected by the deviation between the experimental and theoretical data.

Moreover, the transportation of microplastics (MPs) inside the membrane can be described by the Nernst-Planck equation (ENP):

$$j_i = -K_d D \frac{dc}{dx} + K_c c J_v + \frac{X K_d D}{RT} F \frac{d\psi}{dx} \quad (\text{S5})$$

at $x=0$, $c=c_f$; $x=\Delta x$, $c=c_p$

where J_i is the flux of MPs, D is the diffusivity of water, c is the concentration of MPs in the membrane, x is the distance normal to membrane, K_c is the hindrance factor of convection, J_v is the water flux of membrane, K_d is the hindrance factor of diffusion, F is the Faraday's constant, R is the gas constant, T is the absolute temperature, ψ is the electric potential in axial direction, X is the effective membrane volume charge, c_f is concentration of MPs in the permeate, c_p is concentration of MPs on membrane surface.

The effects of convection ($K_c c J_v$), diffusion ($K_d D \frac{dc}{dx}$), and electric potential ($\frac{X K_d D}{RT} F \frac{d\psi}{dx}$) on the transfer process of MPs within the membrane can be described by modifying **Equation S5** as follows:

$$\frac{dc}{dx} = -\frac{J_v}{K_d D} (K_c c - c_p) + \frac{X}{RT} F \frac{d\psi}{dx} \quad (\text{S6})$$

It can be observed that convection and diffusion affect both the membrane flux and the rejection rate of MPs, while electric potential only affects the rejection rate of MPs and has no impact on membrane flux. This is because MPs are not transported by electric potential through the membrane due to the absence of an electrical potential gradient across it.

The impact of electric potential on the rejection rate through the membrane surface can be described using Donnan-steric partitioning:

$$\frac{c}{c_f} = \left(1 - \frac{r_i}{r_p}\right)^2 \exp\left(-\frac{\zeta_p}{RT} \Delta\psi_D\right) \quad (\text{S7})$$

where r_i is the radius of MPs, r_p is the effective pore radius of the membrane, ζ_p is the zeta potential of the MPs, $\Delta\psi_D$ is the Donnan potential.

The effect of electric potential on the rejection rate within the membrane interior needs to consider the charge density of the membrane (σ^s) is not constant along the pore and its value varies with the axial pore distance, the electric potential inside membrane pore in **Equation S6** can be expressed as:

$$\frac{X}{RT} F \frac{d\psi}{dx} = \frac{J_v}{K_d D} (K_c c - c_p) + \frac{d\sigma^s}{dx} \quad (\text{S8})$$

Generally, it is assumed that the surface charge balances the mobile charges of the electrical double electric layer. Hence, the σ^s of a cylindrical pore wall can be defined as:

$$\sigma^s = -\frac{1}{r_p} \int_0^r F X r dr \quad (\text{S9})$$

Since uniform radial potential is assumed, the radial concentrations of MPs are also constant. Hence **Equation S7** becomes:

$$\sigma^s = \frac{F X r_p}{2} \quad (\text{S10})$$

Assuming the surface electrostatic potential (ψ^s) of the pore wall at the membrane–feed interface, i.e., the Donnan potential at the feed side is equal to the surface electrostatic potential of the isolated surface (assumed to be equal to the zeta potential of particle surface), the surface charge density is related to the zeta potential (ζ_m) through the Gouy–Chapmann equation and, thus, the membrane volume charge (X) can be defined as:

$$X = \text{sign}(\zeta_m) \frac{2}{r_p F} \left(2\varepsilon_r \varepsilon_0 R T c \times \left[\exp\left(-\frac{\zeta_p \zeta_m}{RT}\right) - 1 \right] \right)^{0.5} \quad (\text{S11})$$

Therefore, surface charge density of membrane can be expressed as:

$$\sigma^s = \text{sign}(\zeta_m) \left(2\varepsilon_r \varepsilon_0 R T c \times \left[\exp\left(-\frac{\zeta_p \zeta_m}{RT}\right) - 1 \right] \right)^{0.5} \quad (\text{S12})$$

where ζ_m is the zeta potential on membrane surface, ζ_p is the zeta potential of the MPs, ϵ_r is the dielectric constant of water, ϵ_0 is the vacuum permittivity.

Moreover, assuming the surface charge density of the pore wall is equal to the surface charge density of the isolated surface, the Donnan potential at the feed side is assumed to be equal to the zeta potential, then, the Donnan-steric partitioning can be expressed as :

$$\frac{c}{c_f} = \left(1 - \frac{r_i}{r_p}\right)^2 \exp\left(-\frac{\zeta_m \zeta_p}{RT}\right) \quad (\text{S13})$$

From **Equations S8-13**, it can be determined that the key parameters affecting the rejection rate through electric potential are the zeta potential on the membrane surface (ζ_m), the zeta potential of the MPs (ζ_p), and the effective pore radius of the membrane (r_p). **Figures S12 and S13** demonstrate that the zeta potential on the membrane surface is approximately -78.65 mV, while the zeta potential of the MPs is approximately 0 mV, indicating that electric potential has a limit influence on the mass transfer process of MPs within the membrane. Moreover, **Equation S7** indicates that the closer the size of the MPs is to the size of the membrane pores, the weaker the effect of electric potential on the rejection rate through the membrane surface. In this study, the size of the MPs is relatively close to the size of the membrane pores, therefore, the influence of Donnan-steric partitioning on the rejection rate can be neglected, the rejections of microplastic were mainly controlled by membrane pore size.

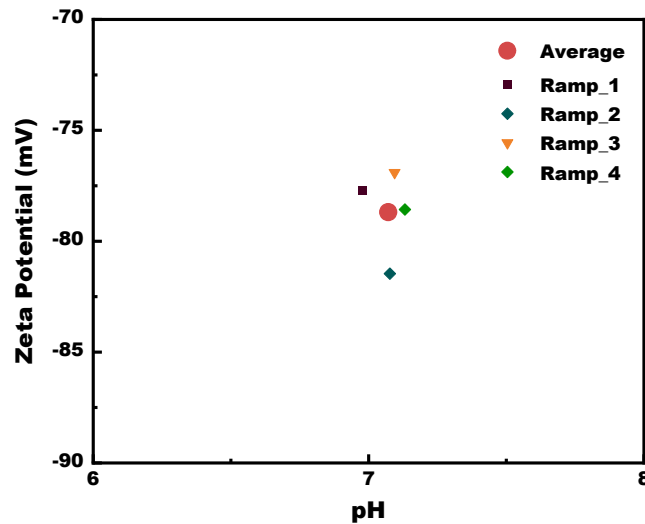


Figure S13. The Zeta potential of the 9-NPs-A5 membrane (ζ_m)

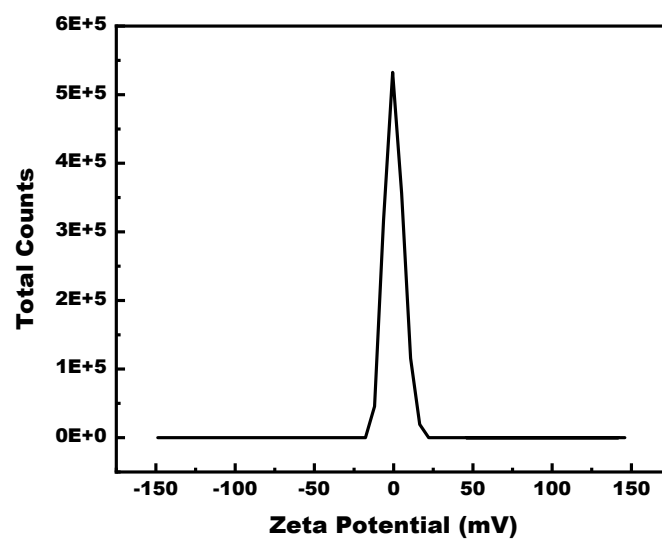
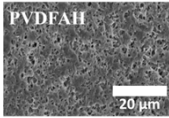
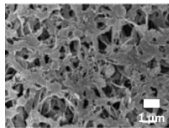
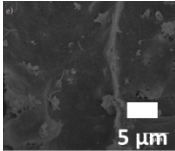
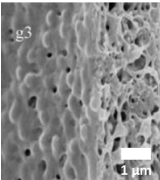
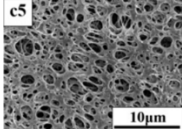


Figure S14. The Zeta potential of the polystyrene (PS) microspheres (ζ_p).

Table S2. Performance comparison of current PVDF-based separation membranes with similar pore size

Membrane	Flux (L·m ⁻² ·h ⁻¹)	Pressure (bar)	Average pore size (nm)	Reference
PVDF-NPs-A5 (This work)	2924.67 ± 28	0.5	523±11	/
PVDF/TA/ NaIO4	5099	1.0	~450	7
PVDF/TA/ PEI	4599	0.5	~150	8
PVDF-PC	3420	1.0	434	9
PVDF/ Zwitterionic hydrogel	~2500	0.1	220	10
PVDF-MWCNT	2137	1.0	420	11
PVDF/Hydrogel	~2000	1.0	 (not given)	12
PVDF -PVP-LiCl	1527.78 ± 411.11	1.0	7709 ± 3.5	13
PVDF-g-PEGMA (DMAc)	1569.42	1.0	798.17	14
PVDF/ MWCNTs/dopamine	1282.5	0.9	 (not given)	15
PVDF/CaCO3	~1250	1.0	280	16
PVDF/LiCl/glycerol	912	1.0	680	17
PVDF-GO-CNC	800	1.0	~1200	18
PVDF-PE-b-PEG	420	1.0	2630	19
PVDF/Phosphorylated silica nanotubes (PSNTs)	251	1.0	 (not given)	20

PVDF-HFP	161.2 ±2.11	1.0	1149.5 ±0.02	21
PVDF (surface- initiated ATRP of HEMA of DMAEMA)	130	1.0	 (not given)	22
PVDF /P(MMA-co- GMA)/ PEI/	90.0 ± 5	0.9	 (not given)	23

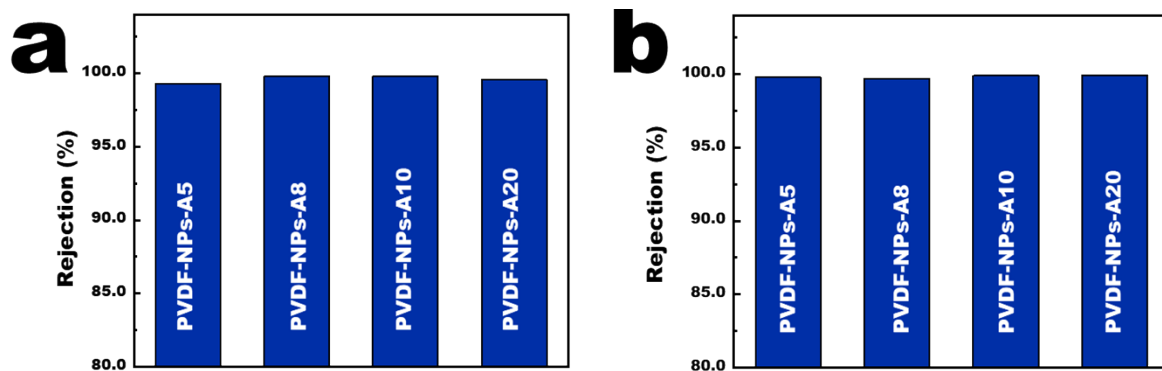


Figure S15. The rejection rates of polystyrene microspheres for the 9-NPs-A membranes. The particle size is 700 nm (a) and 1000 nm (b)

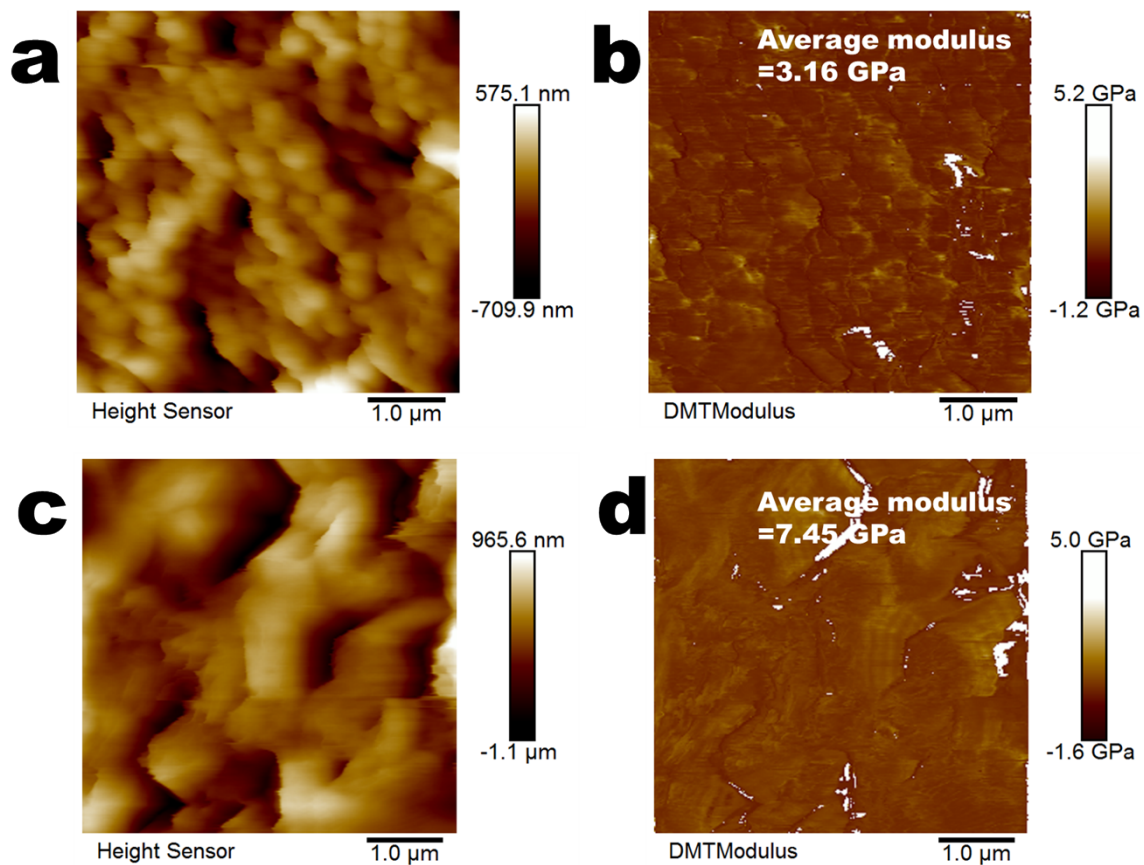


Figure S16. (a, c) AFM images of 9-NPs-A5 membrane (a) and commercial PVDF membrane (c); (b, d) DMT modulus of the 9-NPs-A5 membrane (b) and commercial PVDF membrane (d) (PF-QNM mode, AFM).

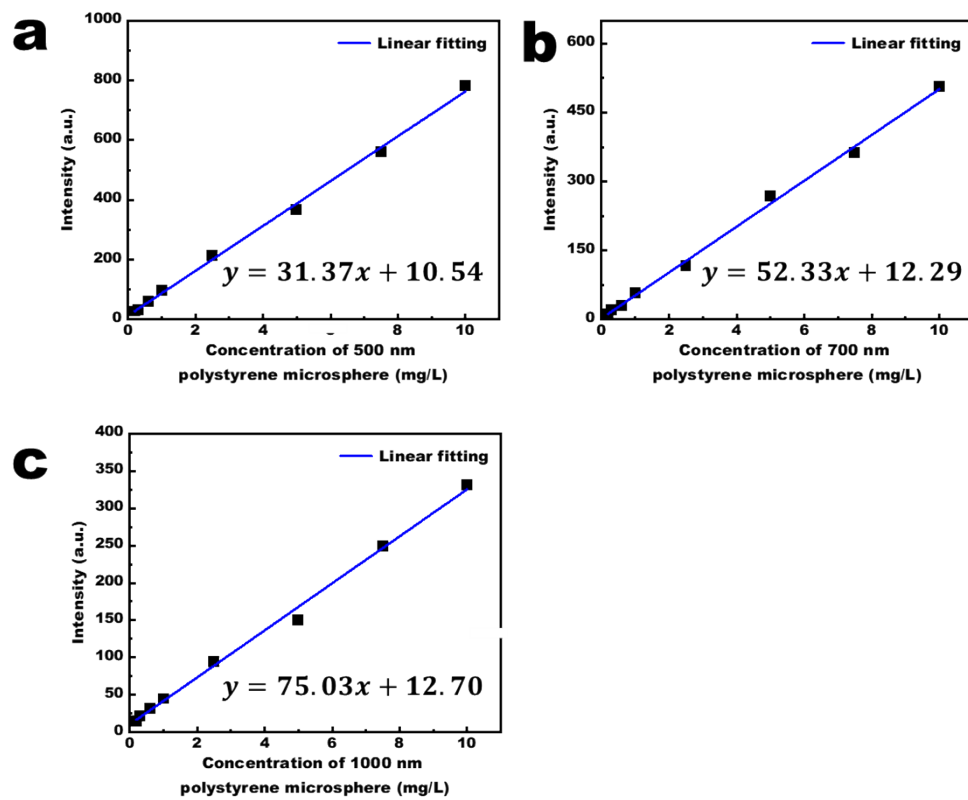


Figure S17. Standard curve of fluorescence intensity at 433 nm versus concentrations of 500 nm (a), 700 nm (b), and 1000 nm (c) polystyrene microspheres.

References

1. J. G. Wijmans and R. W. Baker, *Journal of Membrane Science*, 1995, **107**, 1-21.
2. L. Jin, C.-H. Liu, D. Cintron, Q. Luo, M.-P. Nieh and J. He, *Langmuir*, 2021, **37**, 9865-9872.
3. K. Foroutani, S. M. Ghasemi and B. Pourabbas, *Journal of Membrane Science*, 2021, **623**.
4. F. Algarni, V. E. Musteata, G. Falca, S. Chisca, N. Hadjichristidis and S. P. Nunes, *Macromolecules*, 2021, **54**, 10235-10250.
5. K. Liang, X. Li, L. Wang, Z. Xie, Q. Wang, K. Wang, J. Wu, H. Yu and X. Qiu, *Journal of Membrane Science*, 2023, **669**.
6. Y. Liu, J. Wang, Y. Wang, H. Zhu, X. Xu, T. Liu and Y. Hu, *Chemical Engineering Journal*, 2021, **405**.
7. B. Jiang, K. Cheng, N. Zhang, N. Yang, L. Zhang and Y. Sun, *Separation and Purification Technology*, 2021, **255**.
8. X. Zhao, R. Wang, Y. Lan, T. Wang, J. Pan and L. Liu, *Journal of Membrane Science*, 2021, **630**.
9. R. L. Thankamony, X. Li, X. Fan, G. Sheng, X. Wang, S. Sun, X. Zhang and Z. Lai, *Acs Applied Materials & Interfaces*, 2018, **10**, 44041-44049.
10. Y. Zhu, J. Wang, F. Zhang, S. Gao, A. Wang, W. Fang and J. Jin, *Advanced Functional Materials*, 2018, **28**.
11. H. M. Park, H. Oh, K. Y. Jee and Y. T. Lee, *Separation and Purification Technology*, 2020, **246**.
12. T. Yuan, J. Meng, T. Hao, Z. Wang and Y. Zhang, *Acs Applied Materials & Interfaces*, 2015, **7**, 14896-14904.
13. N. I. M. Nawi, N. R. Sait, M. R. Bilad, N. Shamsuddin, J. Jaafar, N. A. H. Nordin, T. Narkkun, K. Faungnawakij and D. F. Mohshim, *Polymers*, 2021, **13**.
14. Q. Wu, A. Tiraferri, T. Li, W. Xie, H. Chang, Y. Bai and B. Liu, *Acs Omega*, 2020, **5**, 23450-23459.
15. X. Yang, Y. He, G. Zeng, X. Chen, H. Shi, D. Qing, F. Li and Q. Chen, *Chemical Engineering Journal*, 2017, **321**, 245-256.
16. Y. Song, Z. Wang, Q. Wang, B. Li and B. Zhong, *Journal of Applied Polymer Science*, 2016, **133**.
17. J. Lee, B. Park, J. Kim and S. B. Park, *Macromolecular Research*, 2015, **23**, 291-299.
18. J. Lv, G. Zhang, H. Zhang and F. Yang, *Chemical Engineering Journal*, 2018, **352**, 765-773.
19. C. Gandhimathi, S. Sundarajan, T. Matsuura, D. K. Srinivasan, H. Wei, D. Xuecheng and S. Ramakrishna, *Journal of Applied Polymer Science*, 2021, **138**.
20. S. Zhang, R. Wang, S. Zhang, G. Li and Y. Zhang, *Chemical Engineering Journal*, 2013, **230**, 260-271.
21. X. Wang, C. Xiao, H. Liu, Q. Huang and H. Fu, *Journal of Applied Polymer Science*, 2018, **135**.
22. Y. Sui, X. Gao, Z. Wang and C. Gao, *Journal of Membrane Science*, 2012, **394**, 107-119.
23. Y. Deng, G. Zhang, R. Bai, S. Shen, X. Zhou and I. Wyman, *Journal of Membrane Science*, 2019, **569**, 60-70.